Tectonophysics 837 (2022) 229435

Contents lists available at ScienceDirect

Tectonophysics

journal homepage: www.elsevier.com/locate/tecto

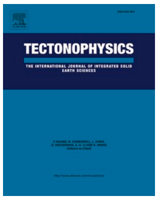

Frictional constitutive behavior of chlorite at low shearing rates and hydrothermal conditions

Benjamin D. Belzer *, Melodie E. French

Department of Earth, Environmental and Planetary Sciences, Rice University, MS-126, 6100 Main Street, Houston, TX 77005, USA

ARTICLE INFO

Keywords:
Rock friction
Experimental rock deformation
Phyllosilicate-rich fault zones
Earthquake mechanics

ABSTRACT

Chlorite is a common, but understudied phyllosilicate mineral along continental and subduction zone faults. To understand the potential role of chlorite in different modes of fault slip, we measure the constitutive frictional properties of chlorite at low rates of deformation and shallow hydrothermal conditions by shearing powdered samples of water-saturated chlorite in the triaxial saw-cut configuration. Experiments were conducted at 25 to 130 °C, 130 MPa confining pressure, pore pressures from 10 MPa to 120 MPa, slip rates from 0.001 to 10 μm/s, and shear displacements up to 7.5 mm. The frictional strength of chlorite increases with increasing temperature from 25 to 130 °C ($\mu = 0.4$ to 0.46), accompanied by an increased abundance of Riedel shears. Chlorite also transitions from rate-strengthening behavior at fast slip rates (0.1 to 10 μm/s) to rate-weakening or rate-neutral behavior at lower slip rates (0.001 to 0.01 μm/s), consistent with one hypothesis for the cause of slow slip. This transition in frictional behavior reflects different microphysical processes controlling the direct and evolution effects of friction. At low deformation rates, the magnitude and temperature sensitivity of the direct effect (a) are consistent with subcritical fracture. In contrast, the evolution effect (b) is insensitive to temperature and increases systematically with decreasing strain rate. We propose the increase in b and resulting rate-weakening behavior of chlorite with decreasing slip rate is controlled by time-dependent properties of adsorbed water to mineral surfaces.

1. Introduction

Fault zones are commonly enriched in sheet silicate minerals (phyllosilicates) that occur in contiguous layers and form by retrogressive or prograde metamorphic reactions (Wintsch et al., 1995). These phases are frictionally weak at subseismic slip rates compared to most types of minerals (Byerlee, 1978) and highly anisotropic in strength because of their layered mineral structures (Kronenberg et al., 1990; Mares and Kronenberg, 1993). The presence of weak, interconnected phyllosilicates is therefore proposed to be a major control on fault strength and strain localization, as well as slip behavior (e.g. Wintsch et al., 1995; Faulkner et al., 2003; Jefferies et al., 2006; Moore and Rymer, 2007; Collettini et al., 2009). As such, understanding the rheological properties of phyllosilicates within fault zones, particularly at in situ pressures, temperatures, and rates of deformation, is important for modeling observed slip modes and improving seismic hazard assessment.

Experimental measurements of the frictional constitutive properties of phyllosilicates at typical laboratory deformation rates (~0.1 to 10 μm/s) show that they typically strengthen with increasing velocity or strain rate, implying that weak faults dominated by phyllosilicates may accommodate aseismic slip (e.g., Scruggs and Tullis, 1998; Saffer and Marone, 2003; Ikari et al., 2009). However, recent deformation experiments have shown that some phyllosilicate-rich fault samples exhibit rate-weakening behavior when sheared at low velocities characteristic of slow slip events (few to few tens of cm/yr) (Ikari and Kopf, 2017; Rabinowitz et al., 2018), challenging the conceptual framework that frictionally weak faults are stable. It is unclear, however, what microphysical processes cause this change in slip behavior at low deformation rates, and whether these mechanisms rely solely on the presence of specific phyllosilicates or additional minerals (e.g., quartz, feldspar) within phyllosilicate-rich gouges (Niemeijer and Spiers, 2007; den Hartog and Spiers, 2013). Although the frictional properties of a wide variety of sheet silicates have been studied at hypocentral temperature and pressure conditions (e.g., Takahashi et al., 2011; Van Diggelen et al., 2010; Lu and He, 2014; Moore and Lockner, 2008; Tesei et al., 2018; Okamoto et al., 2019), fewer monomineralic phyllosilicate samples have been studied at the low shearing velocities representative of slowly

---

* Corresponding author.
E-mail address: bbelzer@rice.edu (B.D. Belzer).

https://doi.org/10.1016/j.tecto.2022.229435
Received 3 March 2022; Received in revised form 2 June 2022; Accepted 6 June 2022

creeping faults (e.g., Reinen et al., 1992; Moore et al., 1997; Scruggs and Tullis, 1998).

An important mineral that remains to be studied at slow in situ rates of deformation is chlorite. Previous studies indicate that chlorite may be a dominant control on fault deformation in many tectonic settings, including basalt-hosted segments of subduction megathrusts, oceanic detachment faults, retrograde faults exhuming mafic rocks, and the deep San Andreas Fault (MacLeod et al., 2002; Schleicher et al., 2012; Fagereng and Ikari, 2020; Braden and Behr, 2021). However, interpretations of its effect on fault zone rheology have been based on previous friction experiments performed using slip rates >0.3 μm/s (Ikari et al., 2009; Okamoto et al., 2019), which show that chlorite has velocity-strengthening friction. As these frictional constitutive properties are largely empirical, it is difficult to reliably extrapolate them to lower rates of deformation.

Here, we report results from triaxial shear experiments on chlorite gouge under hydrothermal conditions and slip rates from 0.001 to 10 μm/s, spanning slow slip rates and the faster velocities previously used to study chlorite deformation. Experiments were conducted at constant confining pressure of 130 MPa, pore fluid pressures from 10 to 120 MPa, and temperatures from ~25 to 130 °C. We determine how the strength, constitutive frictional properties, and microstructure of chlorite vary as a function of velocity, temperature, and effective pressure, finding new evidence that chlorite transitions to rate-neutral and -weakening behavior at low deformation rates. We then use our mechanical and microstructural results to interpret microphysical processes operating within water-saturated chlorite gouge which control transitions in its frictional behavior.

2. Methods

2.1. Sample description

We measured the frictional strength of a fine-grained, chlorite schist that originated from the Michigamme Mine in Michigan, USA and was obtained from Ward's Natural Science. Experiments were conducted on disaggregated schist that was hand-ground with a mortar and pestle and sieved to particles <63 μm in diameter. A hand magnet was used to remove most of the iron oxide minerals from the starting material.

The chemical composition of the sample was measured using a field emission electron probe microanalyzer (EPMA) to collect quantitative wavelength dispersive spectroscopy (WDS) and qualitative electron dispersive spectroscopy (EDS) data. Data were collected at an accelerating voltage of 15 kV and a working distance of 11 mm using a JEOL JXA 8530F Hyperprobe at Rice University. The WDS data were collected from 21 point measurements of chlorite grains at an accelerating voltage of 15.0 kV and current of 5×10^{-8} A (Table S1). EDS measurements were used to identify the oxide phases.

The EPMA measurements of chlorite grains show that our sample has the chemical formula $(Mg_{1.331}Fe^{2+}_{3.282}Al_{1.329}Na_{0.016}Ti_{0.008}Ca_{0.004})(Si_{2.665}Al_{1.335})O_{10}(OH,O)_8$ indicating it is close to chamosite, the Fe^{2+}-rich endmember of the chlorite group. Oxide and phosphate phases were identified from EDS measurements as ilmenite and monazite. Quantitative area analysis of the back-scattered electron images of an experimentally deformed sample shows that it consists of $>97\%$ chlorite with minor amounts of ilmenite and monazite.

2.2. Experimental setup and procedure

We measured the strength and constitutive properties of initially 5 mm-thick layers of disaggregated chlorite using the triaxial sawcut geometry (Fig. 1). Experiments were performed using a servo-controlled triaxial deformation apparatus at Rice University. The apparatus uses a hydraulic pressure system to control confining pressure, pore fluid pressure, and differential load. Confining pressure applies the least compressive stress (σ_3) with silicon oil and pore fluid pressure (P_f) is applied with deionized water at one end of the sample. Confining and pore fluid pressures are measured with an accuracy of 0.01 MPa and LVDTs record displacements of the confining and pore pressure intensifier pistons. Differential load is measured with a temperature-compensated cell internal to the pressure vessel and converted to differential stress (σ_d) by dividing by cross-sectional area of cylindrical forcing blocks. Displacement of the axial piston is recorded with a linear voltage differential transformer (LVDT) external to the vessel and corrected for the elastic distortion of the apparatus using a calibrated stiffness of 2.5×10^8 N/m. External heating bands heat the pressure vessel, and temperature is maintained to within 5 °C of the setpoint using a thermocouple located within the pressure vessel as feedback.

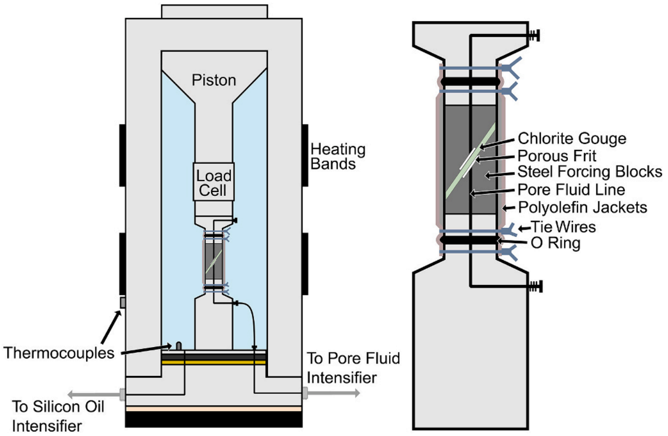

Fig. 1. Schematic of the triaxial deformation apparatus vessel (left) and the saw cut shear configuration (right).

Samples were deformed between cylindrical steel forcing blocks 25.4 mm in diameter with a sawcut surface 35° to the core axis (Fig. 1). The sawcut surfaces have triangular grooves spaced 1 mm apart to promote shear within the gouge layer, and a porous frit 1-mm thick and 13 mm in diameter sit in a recess of the sawcut surface to assist with the distribution of pore fluid at the gouge interface. To prepare each sample, we mixed 12.5 g of chlorite with distilled water to make a thick paste, which we spread in an even layer on one of the blocks using a loading jig and sandwiched carefully with the other block. The sample was then placed between a top and bottom platen and jacketed with three polyolefin sleeves. Once the sample was jacketed and placed in the pressure vessel, confining and pore fluid pressures were increased synchronously to compact the gouge layer yet maintain an effective stress ($\sigma_3' = \sigma_3 - P_f$) less than the target experimental conditions. The experimental setup then equilibrated for 8 to 12 h while the vessel heated overnight, allowing additional time for compaction and for pore pressure to equilibrate across the gouge layer. We measured a thickness of 3.1 mm from a sample that was compacted at 70 MPa effective pressure but not sheared.

We conducted shear experiments at a constant confining pressure of 130 MPa, pore fluid pressures of 10 to 120 MPa, and temperatures of 25 to 130 °C (Table 1). All deformation experiments were initiated with a sliding velocity of 1 μm/s, except for one test (G0176) in which slip was initiated at 0.1 μm/s. After samples yielded and began to show linear strain hardening behavior (with one exception), we performed a series of rate steps at sliding velocities between 0.001 and 10 μm/s, corresponding to shear strain rates of 3×10^{-7} to 3×10^{-3} s^{-1}, to determine the frictional constitutive properties (Dieterich, 1979). Rate steps were imposed every 0.5 mm of slip except during the slowest shear velocity which we held for 0.2 to 0.3 mm of slip. Most chlorite layers were continuously sheared up to 7.5 mm (shear strain of 2.5) which lasted a duration of four days, though in one experiment (G0012) the sample was unloaded after ~4 mm of slip and then reloaded. We conducted two experiments at 120 MPa pore pressure (G0019 and G0202) which

Table 1
List of experimental conditions and strength.

Experiment ID	T (°C)	σ_3 (MPa)	Pf (MPa)	σ_3' (MPa)	λ	V (μm/s)	μ (2 mm)	μ (4 mm)	μ (6 mm)
G0019	130	130	120	10	0.92	1|0.1|0.01|0.001|0.01|0.1|1|10|1|10	0.53	0.57	0.51
G0202	130	130	120	10	0.92	1|0.1|0.01|0.001|0.01|0.1|1|10|1|10	0.48	0.54	0.53
G0012	130	130	60	70	0.46	1|0.1|0.01|0.001|1|10|1|0.1	0.35	0.43	0.44
G0017	130	130	10	120	0.08	1|0.1|0.01|0.001|0.01|0.1|1|10|1|10	0.36	0.42	0.46
G0153	70	130	10	120	0.08	1|0.1|0.01|0.001|0.01|0.1|1|10|1|10	0.34	0.40	0.43
G0110	25	130	10	120	0.08	1|0.1|0.01|0.001|0.01|0.1|1|10|1|10	0.29	0.37	0.40
G0155	25	130	10	120	0.08	1|10|1|	0.35	0.40	
G0176	25	130	10	120	0.08	0.1|0.01|1|	0.33	0.38	

exhibit different strain hardening trends than the other. In G0019 we imposed rate steps at the same strains as other experiments and in G0202 we imposed rate steps at higher shear displacements (4.8 to 10.3 mm) than other experiments. All data was recorded at a sampling rate of 0.2 to 1 Hz for shear velocities of 0.001 to 0.01 μm/s and at 10 Hz for velocities of 0.1 to 10 μm/s.

We used the measured differential stress, confining pressure, and pore fluid pressure to calculate the shear stress, τ, and effective normal stress, σ_n', along the saw cut following standard procedures (e.g., Chester, 1994; Tembe et al., 2010). We corrected our measurements of differential stress for the change in surface area along the saw cut with slip and the strength of our polyolefin jackets (Appendix A). We report the chlorite strength as the friction coefficient, $\mu = \tau/\sigma_n$', assuming zero cohesion consistent with previous studies on gouge friction (e.g., Chester and Higgs, 1992; Marone, 1998). We calculate the displacement along the sawcut from measurements of sample shortening. Volume change of the sample during shear was calculated by multiplying the displacement of the pore pressure intensifier piston by its cross-sectional area.

2.3. Determining rate and state parameters

We use rate-and-state friction constitutive laws to evaluate the effects of slip rate and history on the frictional strength of chlorite (Dieterich, 1979; Ruina, 1983). The common constitutive law for the friction coefficient (μ) is

$$\mu(V,\theta) = \left[\mu_o + a ln\left(\frac{V}{V_o}\right) + b ln\left(\frac{V_o\theta}{D_c}\right)\right] \tag{2}$$

where μ_o is the steady state friction coefficient at a reference velocity V_o, D_c is the critical slip distance required to renew a population of grain contacts, a and b are empirical material parameters indicating the direct and evolution effect, respectively, V is the sliding velocity, and θ is a time-dependent state variable that evolves according to either the aging law (Dieterich, 1979):

$$\frac{d\theta}{dt} = 1 - \frac{V\theta}{D_c} \tag{3}$$

or the slip law [Ruina, 1983]:

$$\frac{d\theta}{dt} = -\frac{V\theta}{D_c} ln\left(\frac{V\theta}{D_c}\right) \tag{4}$$

For steady state slip ($d\theta/dt = 0$), combining and simplifying these equations isolates the rate-dependence of steady-state friction, μ_{ss}, coefficient as:

$$\frac{d\mu_{ss}}{dlnV} = a - b \tag{5}$$

Positive (a-b) values indicate rate-strengthening friction, which promotes stable sliding and fault creep. Negative (a-b) values indicate rate-weakening friction, which is required for the nucleation of unstable slip (e.g., Marone, 1998; Scholz, 2019).

We evaluated the rate and state frictional parameters, a, b, and D_c from our data using an iterative least-squares inversion method (Reinen and Weeks, 1993) and the RSF3000 code developed by Skarbek and Savage (2019). Individual velocity steps were first linearly detrended using 300 μm of slip before each rate step, and data from each rate step was independently inverted across the window 300 μm before and after each step. The data was fit using one state variable and with both the aging (Dieterich) and slip (Ruina) laws. The two friction laws produce similar results (Table S2), and we plot frictional constitutive parameters in this paper using the aging law for comparison with previous experimental literature. Following suggestions by Skarbek and Savage (2019), we treated the sample stiffness as a fitting parameter.

2.4. Transient pore pressure effects

Our ability to quantify the friction coefficient requires that the system is drained, meaning that the pore fluid pressure within the chlorite layer is equal to the pore pressure measured externally. At high shear velocities, pore fluids may become undrained if volume changes in the chlorite outpace the rate that fluids can diffuse into or out of the deforming layer. Following previous studies (e.g., Ikari et al., 2009; Faulkner et al., 2018; Xing et al., 2019) we calculate the time for pore fluid pressure in the gouge to re-equilibrate with the externally measured fluid pressure following a rate step. The characteristic diffusion time is:

$$t = \frac{h^2\beta\eta}{2k}$$

where h is the diffusion length (equal to a gouge thickness of 0.003 m), β is the compressibility of the gouge ($\sim 10^{-10}$ Pa^{-1} following Faulkner et al. (2018)), η is the viscosity of the fluid (0.001 Pa s for water), and k is the permeability of the gouge ($\sim 10^{-20}$ s^{-1} following Morrow et al. (1984), Faulkner and Rutter (2003), Ikari et al. (2009)). Based on these parameters, we calculate that it takes 45 s for pore fluids to equilibrate after a rate step and conclude that deformation must occur over a significantly larger time scale to be considered drained. If we assume that determination of the steady-state friction coefficient requires fluid diffusion over an increment of 150 μm of slip (i.e., one half the displacement following a rate step we use to model frictional behavior), then the maximum slip rate that would allow pore fluid to drain is $v =$ 150 μm/45 s = 3.3 μm/s. This indicates that our fastest rate step (10 μm/s) is likely undrained. In addition, the parameters a, b, and D_c are measured over different time scales, and even slower rate steps could result in undrained conditions over the time scales that these parameters are determined. We measure the individual time intervals over which a, b, and D_c are determined from our data to constrain the slip rates for which these parameters are measured under drained conditions.

2.5. Microstructural analyses

We study the microstructures developed in the chlorite using a combination of polarized light and back-scattered electron (BSE) microscopy. A JEOL JXA 8530F Hyperprobe at Rice University was used to collect BSE images, and this is the same instrument used to determine the chemical composition of the sample. Back-scattered electron images were collected at an accelerating voltage of 15 kV and a working distance of 11 mm.

3. Results

3.1. Frictional strength

The rheology of chlorite is frictional at the experimental conditions as shown by the strong dependence of its shear strength on effective pressure and weak dependence on deformation rate (Fig. 2a). Most of the samples exhibit non-linear strain hardening curves during the initial 2 mm of displacement and gradual near-linear strain hardening for the remainder of shear deformation. The exceptions are the two samples sheared at the lowest effective pressure (10 MPa; G0019 and G0202), which initially strengthen with increasing strain but then strain-weaken to a residual strength. Across all samples, friction coefficients range between 0.29 and 0.53 at 2 mm of shear displacement and 0.40 and 0.53 at 6 mm of displacement (Fig. 2b and c). At 6 mm displacement and 130 °C, the friction coefficient is similar ($\mu = 0.44$ and 0.46) for samples sheared at effective pressures of 120 and 70 MPa corresponding to 10 MPa and 60 MPa pore fluid pressure, respectively, but is higher ($\mu = 0.5$) at the lowest effective pressure of 10 MPa corresponding to 120 MPa pore pressure. At constant effective pressure of 120 MPa, the frictional strength of the chlorite increases with increasing temperature from $\mu = 0.40$ at room temperature (25 °C) to $\mu = 0.46$ at 130 °C (Fig. 3).

3.2. Volume change

The chlorite samples compact during shear until 3 to 4 mm of displacement, after which they deform at a relatively constant pore volume (Appendix B). Comparison of pore volume change as a function of displacement and time over the course of multiple rate steps shows that compaction is controlled by displacement and not deformation rate (Fig. B.1). As a result, at displacements <3 to 4 mm, there is an increased

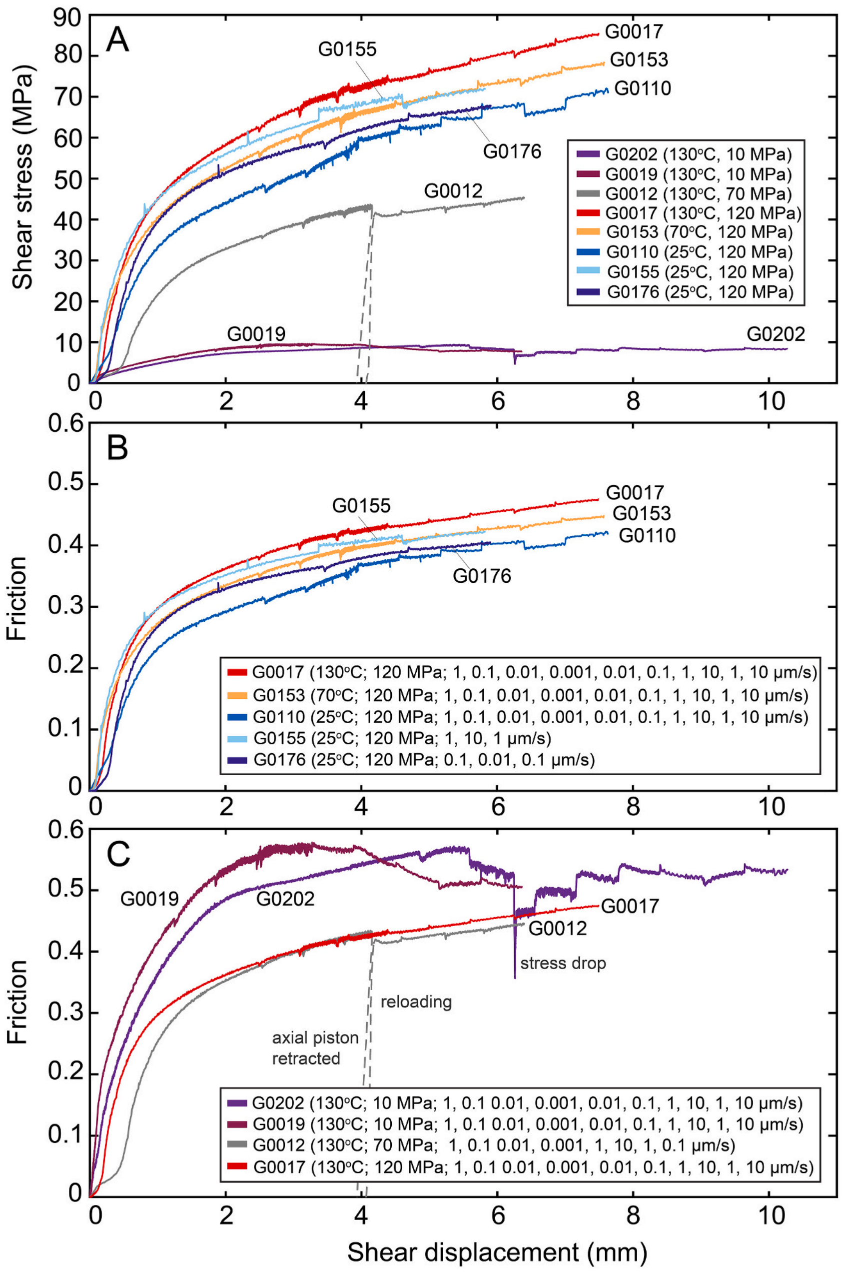

Fig. 2. Mechanical results from shear experiments on chlorite. (a) Shear stress plotted as a function of shear displacement for all experiments (Table 1). In experiment G0012, an experimental error caused the axial piston to be retracted at ~4 mm displacement. It was then advanced to continue shearing. A different internal load cell was also used in experiments G0155 and G0176 than in the rest of the experiments. (b) Friction (shear stress divided by effective normal stress) as a function of shear displacement for experiments conducted at 120 MPa effective pressure and different temperatures. (c) Friction as a function of shear displacement for experiments conducted at 130 °C and different effective pressures.

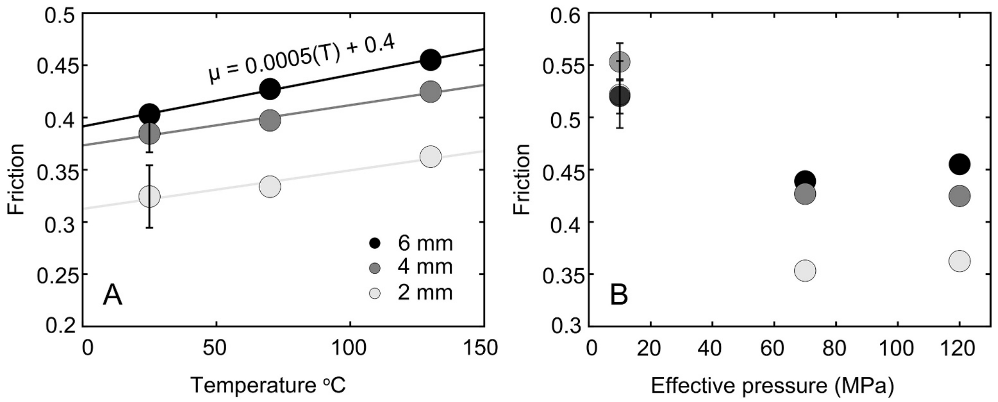

Fig. 3. (a) Friction coefficient at different temperatures for 120 MPa effective pressure and different shear displacements (G0110, G0155, G0176, G0153, G0017; Table 1), (b) Friction coefficients at different effective pressures at 130 °C and different shear displacements (G0019, G0202, G0012, G0017; Table 1).

rate of compaction with time as velocity increases. We are only able to document these effects at velocities of 1 and 10 μm/s. At lower velocities changing environmental factors in the laboratory (e.g., the room temperature) have a more pronounced effect on the pore pressure intensifier piston LVDT, which masks measurements of the small volume changes in the sample.

3.3. *Velocity dependence of the frictional strength*

Chlorite deformed at room temperature (25 °C) shows a clear transition from rate-weakening (a-b = −0.004) at slow velocities (0.001–0.1 μm/s) to rate-strengthening (a-b = 0.005) at fast velocities (1–10 μm/s) (Fig. 4a). In contrast, at 70 and 130 °C and the same effective pressure (120 MPa) the frictional strength is near rate-neutral across the range of slip velocities tested (Fig. 4a and b), although at 130 °C the chlorite shows a trend consistent with a transition from slightly rate-weakening (a-b = −0.001) to slightly rate-strengthening (a-b = 0.001) over a 4 orders of magnitude increase in velocity (Fig. 4a).

At 130 °C, the rate-dependence of the frictional strength is similar at 120 MPa and 70 MPa effective pressure, exhibiting a transition from slightly rate-weakening to slightly rate-strengthening with increasing slip rate (Fig. 4c). In contrast, at 10 MPa effective pressure ($P_f = 120$ MPa), the frictional behavior of chlorite shows much greater variability with respect to slip rate, shear displacement, and step direction which makes identifying clear trends challenging. Overall, at velocities <1 μm/s the chlorite rate-strengthens significantly (a-b = 0.008 to 0.016) when rate steps were imposed beyond ~5.5 mm of slip (G0202), but has rate-neutral strength when imposed at lower displacements (G0019). In addition, at 10 MPa effective pressure chlorite generally rate-weakens between 1 and 10 μm/s, as shown most prominently when the velocity is stepped down from 10 to 1 μm/s (a-b = −0.009 to −0.015). We infer though that the rate-weakening behavior at high velocities may result from transient fluid overpressure in the sample, based on our estimate that slip rates >3.3 μm/s result in undrained conditions and observations of compaction during those fast slip rates (Appendix B).

The parameters *a* and *b* vary with temperature and deformation rate (Figs. 5 and 6). At room temperature, *a* increases with velocity, while at 70 °C and 130 °C a trend is not as clear (Fig. 5a b). In addition, *a* increases with increasing temperature at slow velocities (0.001 to 0.01 μm/s) yet shows the reverse trend at faster velocities (0.10 to 10.0 μm/s) (Fig. 6a and b). These trends indicate that the processes controlling the direct effect in chlorite are temperature- and time-sensitive. The parameter *b* shows more consistent behavior; across all velocities and in all experiments except at very high pore pressure, *b* decreases systematically with increasing velocity such that at the fastest velocity (10 μm/s) *b* becomes very low or zero (b = 0 to 0.002) (Fig. 5c and d). However, *b* is generally less sensitive to temperature compared to *a*, as *b* only increases between 70 °C and 130 °C when the velocity is stepped down to 0.01 and 0.001 μm/s (Fig. 6c and d). Values of *Dc* are more scattered but are greatest at room temperature and increase slightly with increasing velocity at 70 °C and 130 °C (Figs. 5e and f and 6e and f). The parameters *a*, *b*, and *Dc* do not show clear trends with increasing effective pressure during rate steps imposed at similar amounts of slip.

We determine the time scales over which *a, b,* and *Dc* are measured at different velocities to evaluate whether the reported values reflect deformation under drained conditions. We previously determined that at velocities up to 3.3 μm/s steady-state strength is measured under drained conditions, and we conclude that *b* and *Dc* are also measured under drained conditions at these velocities. Specifically, the time interval over which *b* and D_c are measured exceeds 45 s at velocities between 0.001 and 1 μm/s, except when the sample is heated and sheared at 1 μm/s. In contrast, the 'instantaneous' rate dependence (*a*) is measured over a much shorter time scale; approximately 1% (3 μm) of the slip following a rate step controls the inverse model result for *a*. Accordingly, deformation associated with the measurement of *a* only exceeds the equilibration time of 45 s at velocities up to 3 μm /45 s = 0.07 μm/s, and rate steps between 0.1 and 10 μm/s provide measurements for *a* under undrained conditions. Our observations of compaction at these rates indicate that these steps may induce transient fluid overpressure, thereby decreasing the value of *a* (Faulkner et al., 2018). The values of *a* that we report at these rate steps are thus lower bounds, which we consider in our interpretations of the data.

3.4. *Microstructures*

All deformed chlorite layers that were examined developed shear bands that define composite planar fabrics (Fig. 7). The shear bands are a few tens of microns wide and have R_1- and Y-orientations following the terminology of Logan et al. (1979), although R_1-shears are generally more common. Within shears grain size reduction has occurred, and both R_1- and Y- shears contain strongly aligned grains of chlorite, as indicated by the uniform birefringence colors in cross-polarized light with and without the gypsum wedge inserted. The occurrence and distribution of these shears varies with the effective pressure and temperature of deformation.

Boundary shears develop near the forcing block contacts at all conditions in the Y-orientation (Fig. 7). Y-shears also occur through the center of chlorite layers deformed at the highest effective stress, spanning nearly the entire length of the samples (G0110 and G0017), but not at the lowest effective stress (G0019). The R_1 shears locally anastomose, split, and connect with adjacent R_1- and Y-shears. The abundance of R_1 shears varies strongly with effective pressure and temperature. Increasing effective pressure results in the formation of a greater abundance of R_1 shears, as can be seen by comparing samples deformed

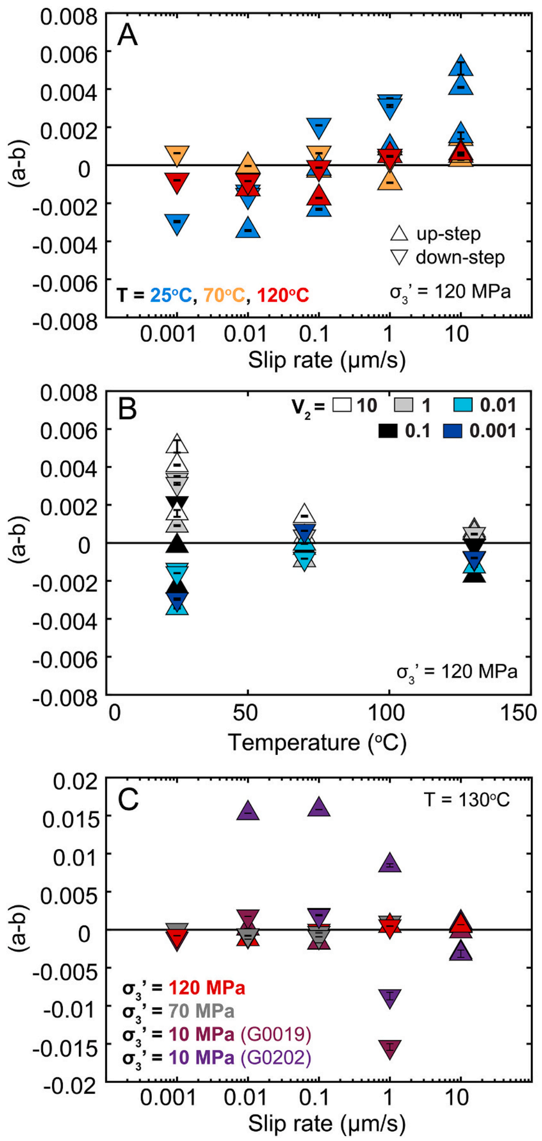

Fig. 4. Rate-dependence of chlorite frictional strength (a) as a function of slip rate for experiments at 120 MPa effective pressure and different temperatures (G0110, G0155, G0176, G0153, G0017; Table 1), (b) as a function of temperature at an effective pressure of 120 MPa and for different rate steps (G0110, G0155, G0176, G0153, G0017; Table 1), and (c) as a function of slip rate for experiments at 130 °C and different effective pressures (G0019, G0202, G0012, G0017; Table 1), The *a-b* values are plotted at the final velocity for each step; up arrows indicate the slip rate increased and down arrows indicate slip rate decreased.

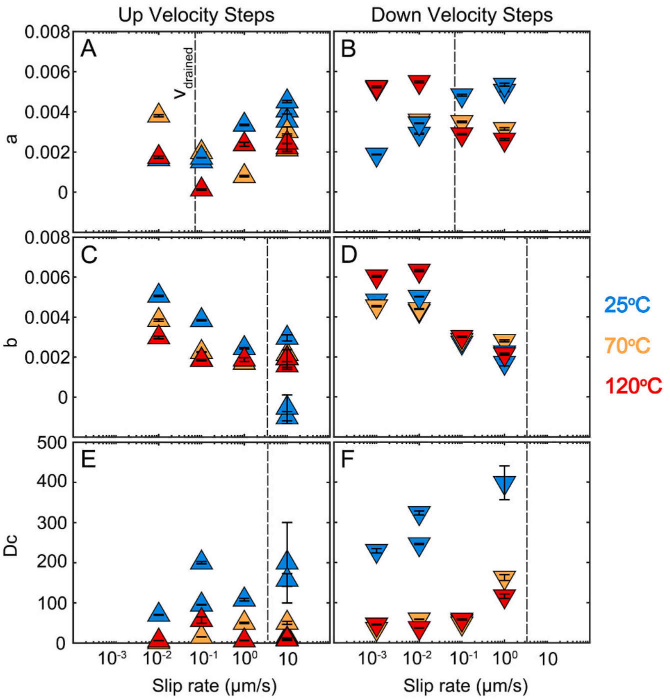

Fig. 5. Variations in the rate and state friction parameters *a*, *b*, and *Dc* as a function of slip rate for shear experiments conducted at 120 MPa effective pressure and 25, 70, and 130 °C (G0110, G0155, G0176, G0153, G0017; Table 1). Results for steps up and down in velocity are shown separately with arrows pointing up and down, respectively. Slip rates correspond to the velocity stepped to during the experiment. Error bars represent 2σ, where σ is the standard deviation of the fitted parameter values. Dashed vertical lines indicate the maximum velocities that provide measurements for *a*, *b*, and *Dc* under drained conditions. Parameters were fit using the aging friction relation (Skarbek and Savage, 2019; Dieterich, 1979).

at 130 °C and either 10 MPa effective pressure (G0019), which exhibits only a few thin shears spaced throughout the layer, or 120 MPa effective pressure (G0017), which exhibits a much greater abundance of shear bands (Fig. 7a and b). The abundance of R_1 shears also increases with temperature. Among the samples deformed at 120 MPa effective pressure, a large number of distributed shears developed at 130 °C (G0017), whereas at 25 °C (G0110) deformation is concentrated more strongly within tabular zones of R_1 shears (Fig. 7b–e). The increase in R_1 shear abundance with increasing temperature or pressure also correlates with higher shear strength. We also see fewer and more localized shears in chlorite deformed at higher velocities that correspond to rate-strengthening (G0155) behavior compared to lower velocities and rate-weakening (G0176) frictional behavior (Fig. 7d and e).

Although deformation is predominantly accommodated along localized shears, the deformed samples also display more developed foliation with increasing effective pressure (Fig. 8a and b). The foliation is defined by elongated grains of chlorite and magnetite, which are inclined in the P-orientation 20-30° from the saw-cut angle in samples sheared at 120 MPa effective pressure. Individual grains of chlorite exhibit bending, kinking, and undulose extinction, which are crystal plastic deformation mechanisms (Fig. 8b and c). However, chlorite grains within the original undeformed schist also display these microstructures, so it is difficult to assess from our thin sections whether crystal plastic mechanisms operated during our deformation experiments.

4. Discussion

4.1. Frictional strength

We document the frictional strength of Fe-rich chlorite gouge with shear displacement (shear strain), effective pressure, temperature, and sliding velocity. Shear displacement has a large influence on strength as most samples show significant strain hardening behavior (Fig. 2; Table 1). This behavior may occur because we use a relatively thick gouge layer (~3 mm after compaction), which could require high shear displacements to reach a shear strain required for steady-state frictional sliding. Shear experiments on initially 1 mm thick phyllosilicate gouge layers, by comparison, typically do not show as extensive strain hardening (e.g., Morrow et al., 2000; Moore and Lockner, 2011). The strain hardening trends we observe during experiments at 70 and 120 MPa effective pressure may reflect continuous grain crushing during shear consistent with results from Haines et al. (2013) who showed similar strain hardening trends that correlated with evidence of significant grain

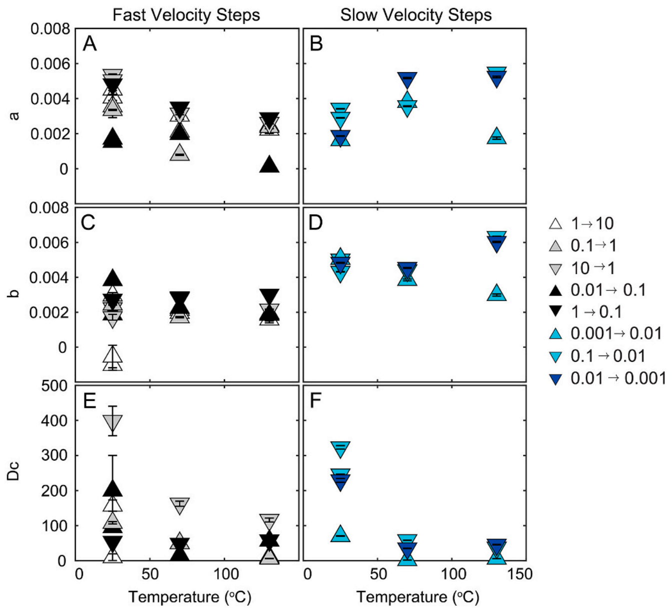

Fig. 6. Variations in rate and state friction parameters *a*, *b*, and *Dc* as a function of temperature at an effective pressure of 120 MPa (G0110, G0155, G0176, G0153, G0017; Table 1) and fit using the aging law. Values for the fast range of velocity steps (0.1–10 μm/s) are plotted in the left column and those at slow velocity steps (0.001–0.01 μm/s) are plotted in the right column. Results for steps up and down in velocity are shown separately with arrows pointing up and down, respectively. Slip rates correspond to the velocity stepped to during the experiment.

size reduction in crushed chlorite schist, but steady-state frictional sliding in finer natural gouge chlorite (<2 μm) with minimal change in particle size distribution with increasing shear strain.

Even with strain hardening, the range of friction coefficients that we report at room temperature and 70–120 MPa effective pressure is generally comparable to the steady-state friction coefficients of 0.2 to 0.4 reported for saturated chlorite-rich gouges at room teimperature (Fagereng and Ikari, 2020; Behnsen and Faulkner, 2012; Ikari et al., 2009; Moore and Lockner, 2004; Morrow et al., 2000). Furthermore, our observation of a greater steady-state friction coefficient ($\mu = 0.52$) at 10 MPa effective pressure is consistent with studies showing higher friction coefficients at very low effective normal stress in clays and other sheet silicates due to non-negligible cohesion (e.g., Behnsen and Faulkner, 2012). Differences in the friction coefficients reported from different studies on chlorite may result from several factors including the presence of additional phases within samples, grain size distribution and geometry, different experimental conditions, the use of simulated gouge versus natural cataclasite or single crystal sheets (Smith et al., 2017; Okamoto et al., 2019), and the chemical composition of chlorite (Moore and Lockner, 2015). Our measured friction coefficients for Fe-rich chlorite (chamosite) are slightly higher than the steady-state value of 0.38 measured for ripidolite, which has an intermediate Mg/Fe ratio, at room temperature (Moore and Lockner, 2004). Clinochlore, which is the Mg-rich endmember of chlorite and forms a solid solution series with chamosite, has an even lower steady-state friction coefficient of 0.25 at room temperature (Okamoto et al., 2019). Our sample of chamosite contains 35 wt% FeO, compared to 5 wt% FeO in the clinochlore used by Okamoto et al. (2019). Our results therefore support the observation that increasing Fe content in chlorite promotes a slight increase in its frictional strength (Moore and Lockner, 2015). Additionally, the frictional strength of our chlorite gouge sample is greater than that of intact chlorite-rich cataclasite (Smith et al., 2017) and significantly higher than sheared stacks of single chlorite sheets (Okamoto et al., 2019). This is in agreement with previous studies that have demonstrated that samples with well-developed foliation or artificially aligned phyllosilicate sheets can be significantly weaker than powdered samples (e.g., Collettini et al., 2009; Carpenter et al., 2012; Tesei et al., 2012; Kawai et al., 2015; Okamoto et al., 2019). Thus, the friction coefficients that we report on simulated chlorite gouge likely provide an upper bound for strongly aligned, interconnected networks of chlorite within natural faults.

The increase in chlorite frictional strength with temperature that we document has also been documented in illite and lizardite (Moore et al., 1997; den Hartog et al., 2012; Kubo and Katayama, 2015), though lizardite has been shown to exhibit temperature-neutral friction as well (Tesei et al., 2018). In contrast, other sheet silicate-rich fault rocks including talc and smectite weaken with increasing temperature (Moore and Lockner, 2008; Coble et al., 2014). Some previous studies on phyllosilicate-rich fault gouges have attributed the strengthening effect of temperature to the thinning of water films adsorbed to mineral surfaces (e.g., Kubo and Katayama, 2015; Okamoto et al., 2019) which can act as a lubricant during shear in water-saturated and room dry experiments (e.g., Moore and Lockner, 2004; Behnsen and Faulkner, 2012; Sánchez-Roa et al., 2017; Beynon and Faulkner, 2020). In accordance with site adsorption theory (Masel, 1996), an increase in temperature is expected to reduce the thickness of adsorbed water films and therefore increase the shear resistance between mineral surfaces (Israelachvili et al., 1988). In other cases, temperature-strengthening frictional behavior has been attributed to thermally activated mechanisms of the minerals, such as subcritical crack growth (Chester, 1994). However, when controlled by mineral deformation, strengthening is usually very small, on the order of the rate-dependence of strength, and best measured using temperature-stepping experiments (Chester, 1995). We measure a relatively strong effect of temperature (Fig. 3), and as a result we infer the temperature dependence of strength that we measure is likely controlled by the strength of water films.

In our study, higher temperature correlates with a clear increase in the number and density of shears that develop (Fig. 7), which also correlates with a corresponding increase in shear strength (Figs. 2a). Additionally, higher Riedel abundance and shear strength correlate with increasing effective pressure. We interpret that the greater abundance of shears at elevated temperature and pressure reflects the decrease in water film thickness (i.e., number of water monolayers) between aligned sheets of chlorite. If structured water films are initially thinner due to elevated temperature or pressure, then less slip is required to subsequently thin or squeeze them out between aligned plate surfaces. This would cause individual shears to strengthen more readily with slip, and in turn, distribute deformation to weaker layers in the gouge where more shear surfaces would develop. An increase in Riedel shear abundance with increasing temperature and strength has also been reported in illite-rich gouge when sheared from room temperature to 200 °C (Kubo and Katayama, 2015). However, from 200 to 600 °C, the distribution of Riedel shears in illite generally remains constant with increasing temperature (Moore et al., 1989). Thus, the correlation we observe in our study between increasing temperature and Riedel shear abundance may only extend to low temperature ranges (<200 °C) in some phyllosilicates.

4.2. Rate and state dependence of strength

The rate dependence of chlorite frictional strength (*a-b*) exhibits complex correlations with slip rate and temperature at the experimental conditions (Fig. 4a). The chlorite gouge rate-strengthens when sheared at fast slip rates (1–10 μm/s), except during the tests at the lowest effective pressure (G0019 and G0202), during which it was likely that compaction produced fluid overpressure at fast velocity steps leading to apparent rate-weakening (Faulkner et al., 2018). This is consistent with earlier studies that have documented rate-strengthening behavior of chlorite over a similar range of velocities (Ikari et al., 2009; Haines et al., 2013; Okamoto et al., 2019; Fagereng and Ikari, 2020). However, at the

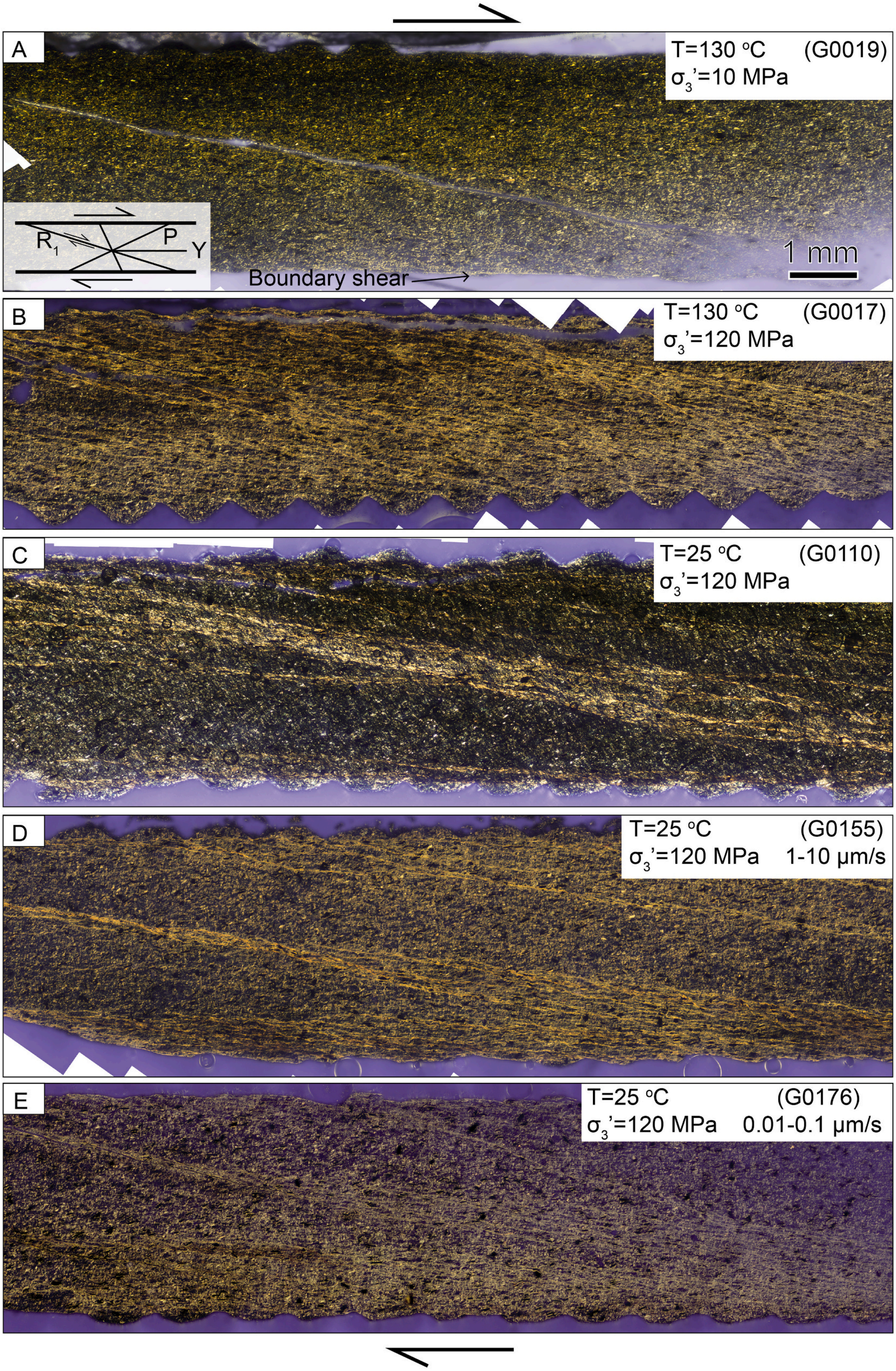

Fig. 7. Cross-polarized light photomicrographs of deformed samples oriented parallel to slip direction at (a) 130 °C and 10 MPa effective pressure, (b) 130 °C and 120 MPa effective pressure, and (c-e) 25 °C and 120 MPa effective pressure. (d and e) Samples deformed at only 1–10 μm/s and 0.01–0.1 μm/s, respectively. Shear band orientations based on the convention of Logan et al. (1979).

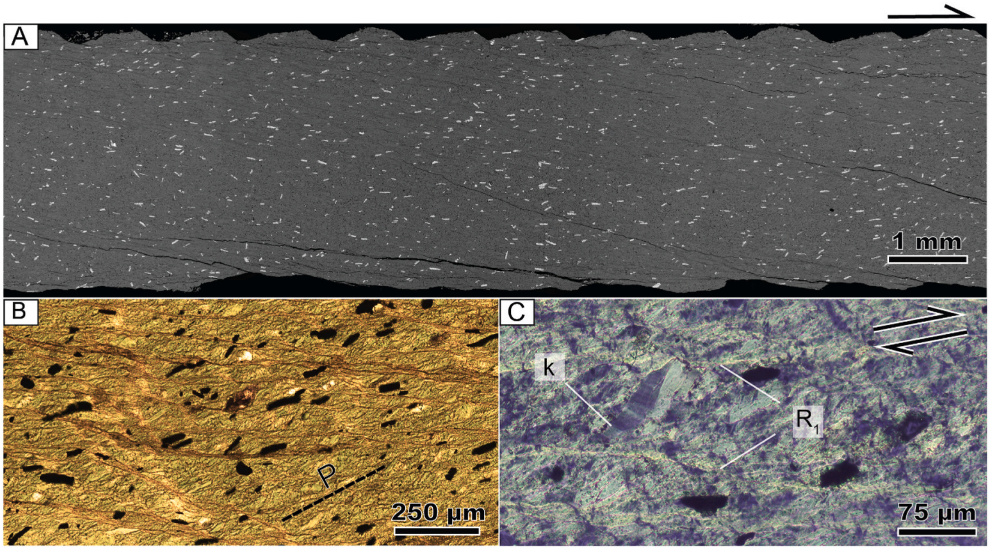

Fig. 8. Characteristic microstructures of chlorite gouge layer. (a) BSE image of a chlorite sample deformed at 25 °C and 120 MPa (G0110) displaying alignment of ilmenite grains subparallel with shear direction (top-right). This image was used to quantify abundance of minor phases (i.e., ilmenite) in the experimental samples. (b) Plane polarized light photomicrograph of G0110 showing alignment of ilmenite and chlorite grains in a P-orientation (20-30° to the saw-cut angle). (c) Cross polarized light photomicrograph of sample deformed at 130 °C and 120 MPa (G0017) with rotated chlorite grain between R_1-shears displaying kink bands (k) and twinning; shear direction indicated in upper right.

lower sliding velocities (0.001–0.1 μm/s) used in our study, chlorite exhibits predominantly rate-neutral or rate-weakening behavior, except when sheared under very high pore fluid pressure. The transition from negative to positive values of (*a*-*b*) with increasing velocity is sometimes referred to as the cutoff velocity (e.g., Shibazaki and Iio, 2003), and it occurs at ~1 μm/s and is most dramatic at room temperature. The cutoff velocity of chlorite reflects different dependencies of the direct and evolution effects on velocity and temperature.

The contact-scale model of frictional deformation proposed by Chester (1994) predicts that rate-weakening friction occurs at the same conditions as temperature-strengthening friction and vice versa if the direct and evolution effects are governed by the same micromechanical process. This correlation between temperature and velocity-dependent frictional strength has been observed in studies on quartzofeldspathic and phyllosilicate-rich gouges (e.g., Chester, 1994; Blanpied et al., 1998; Moore and Lockner, 2008; den Hartog et al., 2012; Coble et al., 2014). However, in contrast to this model our results demonstrate that (1) chlorite rate-strengthens at the same velocities (1–10 μm/s) at which its frictional strength increases with temperature and (2) the direct and evolution effects show different dependencies on slip rate and temperature. This implies that different contact-scale processes may be controlling the direct and evolution effects of friction at the conditions of our study.

Previous experimental data on phyllosilicates at low deformation rates show a correlation between the temperature dependent frictional strength and rate-dependence that is consistent with the Chester (1994) model. At room temperature and very low sliding velocities (~0.001 to 0.01 μm/s), water-saturated chrysotile, talc, and smectite gouges all show rate-strengthening behavior and weaken with increasing temperature between 25 and 100 °C (Moore et al., 1997; Moore and Lockner, 2008; Coble et al., 2014). Thus, the frictional strength and rate-dependence of these phyllosilicates are thought to depend on mineral deformation at sliding velocities below 0.01 μm/s. Antigorite, biotite, and muscovite similarly rate-strengthen at these low velocities (Reinen et al., 1992; Scruggs and Tullis, 1998). However, their frictional strength is insensitive to temperature between 25 and 100 °C (Takahashi et al., 2011; Lu and He, 2014; Van Diggelen et al., 2010), which suggests the Chester (1994) model may not describe the dominant physical properties of some phyllosilicates.

In contrast to the phyllosilicates discussed above, some lizardite and illite gouges have been reported to strengthen with increasing temperature above 25 °C (Moore et al., 1997; Kubo and Katayama, 2015), yet the rate-dependencies of these minerals at low velocities are not well constrained. Moore et al. (1997) reported rate-weakening behavior of lizardite at velocities between ~0.03 and 1 μm/s but acknowledged a general lack of repeatability in their data. However, despite this gap in experimental data, previous studies indicate that illite-rich gouges are also rate-neutral or rate-weakening at low velocities, even at low temperatures (den Hartog et al., 2012; Ikari and Kopf, 2017; Rabinowitz et al., 2018). For example, den Hartog et al. (2012) showed that illite gouge transitions from rate-strengthening to rate-weakening at temperatures between 200 and 300 °C for sliding velocities between 1 and 100 μm/s. They observed that the *a-b* values of illite systematically decrease with decreasing velocity, and thus proposed that extrapolating their *a-b* data to lower velocities would shift the rate-weakening behavior of illite to lower temperatures, consistent with our results on chlorite. Additionally, Rabinowitz et al. (2018) documented the effects of velocity and temperature on the frictional properties of carbonate- and clay-bearing sediment subducting at the Hikurangi Trench. They reported that its strength increases from 20 to 100 °C and found that the sediment transitioned to rate-weakening behavior at plate-rate velocities. Although clay minerals made up only ~20% of their sample, they interpreted that the clay fraction predominantly controlled the frictional strength and behavior. Thus, it is possible that the processes controlling the temperature and rate dependencies of strength in our chlorite sample are similar in other phyllosilicates such as illite.

4.2.1. Micromechanical controls on the direct effect

At low sliding velocities (0.001–0.01 μm/s), the increase in *a* with increasing temperature is consistent with previous studies on several minerals including olivine, plagioclase, antigorite, biotite, and smectite that show a linear increase in *a* with increasing temperature (Fig. 6b) (King and Marone, 2012; He et al., 2013; Takahashi et al., 2011; Lu and He, 2014; French et al., 2015). This behavior is commonly interpreted to reflect a thermally activated deformation mechanism that controls deformation at grain contacts (Chester, 1995; Rice et al., 2001; Nakatani, 2001; Beeler et al., 2007), such as dislocation glide in phyllosilicates (Beeler et al., 2007; Lu and He, 2014; French et al., 2015). Tullis and Weeks (1987) and Beeler et al. (2007) developed a normalization scheme that relates the magnitude of *a* to the rate-dependence of the contact scale deformation mechanism given by $a_0/\mu_0 = A_{c0}/\tau_0$, where the subscript 0 refers to reference temperature and strain-rate conditions, a_0 is the frictional rate dependence, μ_0 is the reference friction coefficient, A_{c0} is the rate-dependence of the contact scale deformation mechanism, and τ_0 is the contact scale shear stress.

We evaluate whether our data for chlorite are consistent with previous analyses for phyllosilicates. For our chlorite sample, we approximate $a_0 = 0.0045$ and $\mu_0 = 0.42$ at 100 °C and 10^{-1} s^{-1} with a resulting ratio of $a_0/\mu_0 = 0.011$. Although dislocation glide data for chlorite are not available, the normalized rate dependence for illite, biotite, and muscovite range between 0.014 and 0.018 when scaled to 100 °C and 10^{-1} s^{-1} (French et al., 2015). This is larger than the normalized rate-dependence of chlorite friction. For comparison, a_0/μ_0 of smectite gouge at velocities $<10^{-5}$ μm/s (shear strain rates less than $\sim 5 \times 10^{-9}$ s^{-1}) is 0.017 ± 0.03 and inferred to reflect dislocation glide; however, at velocities $>10^{-5}$ μm/s, $a_0/\mu_0 = 0.009 \pm 0.003$ and is inferred to reflect subcritical delamination and fracture (French et al., 2015). By comparison, we infer that the similar normalized rate dependence over a similar range of velocities ($> 10^{-5}$ μm/s) is most consistent with the occurrence of the same mechanism, subcritical fracture and delamination, in chlorite as well, although this comparison does not rule out the operation of additional deformation mechanisms.

Microstructural evidence of grain size reduction is consistent with our inference that the instantaneous rate dependence (a) is controlled by subcritical fracture. Evidence of crystal plastic deformation of individual chlorite grains, including undulatory extinction, kinking, and twinning (Fig. 8), may have only been inherited from the original chlorite schist and may not have occurred during frictional shear. However, crystal plasticity could control the rate-dependence at lower velocities and higher temperatures as has been inferred in other phyllosilicates (e.g., Reinen et al., 1992; Scruggs and Tullis, 1998; Beeler et al., 2007; French et al., 2015).

At the faster velocity steps between 0.1 and 10 μm/s, the decrease in a with increasing temperature is not consistent with any thermally activated deformation mechanism of the mineral, suggesting that other microphysical processes control the direct effect during these fast slip rates. We note that at similar velocities, the magnitude of a in montmorillonite increases with increasing hydration state while its coefficient of friction decreases (Ikari et al., 2007). For montmorillonite, this corresponds to both the number of water interlayers and the amount of water adsorbed onto crystal surfaces, though much of the water is adsorbed to surfaces of montmorillonite due to its high specific surface area (Newman, 1987; Moore and Lockner, 2007). Thus, although chlorite does not adsorb water molecules in its interlayer space (i.e. is a non-swelling clay), the removal of adsorbed water from chlorite surfaces may similarly decrease the direct effect with increasing temperature.

4.2.2. *Micromechanical controls on the evolution effect*

In contrast to the direct effect, the evolution effect does not demonstrate a clear dependence on temperature but is sensitive to deformation rate. The systematic decrease in the magnitude of b with increasing slip rate is the main driver of rate-weakening behavior at low velocities in our study. The b parameter is thought to reflect the evolution of grain contact area or strength through physical or chemical processes (Dieterich and Conrad, 1984). Studies of saturated clay-rich fault gouges, including illite, montmorillonite, talc, and chlorite, report negligible or negative b values with $a\text{-}b > 0$, indicating that the real area of mineral contact does not vary significantly with shearing velocity (Moore and Lockner, 2008; Ikari et al., 2009). In experiments above 10 MPa effective pressure, we only observe near-zero values of b at the fastest velocity steps (Fig. 5c and d), which suggests that time-dependent processes controlling the evolution effect are important at low strain rates. Like our chlorite sample, biotite and muscovite gouges also exhibit $b > 0$ (e.g., den Hartog et al., 2013; Lu and He, 2014).

Several deformation mechanisms have been proposed to explain the rate-weakening behavior of phyllosilicate-bearing fault rocks at either low slip rates or high temperatures. These include: (1) time-dependent removal of adsorbed water films (Scruggs, 1997), (2) time-dependent plastic deformation at grain-scale asperity contacts, which increase growth in real areas of contact (Dieterich, 1981; Ikari and Kopf, 2017), (3) thermally-activated deformation of clasts (e.g., quartz and calcite) by pressure solution or stress corrosion cracking, with athermal granular flow of the gouge layer accompanied by dilation (Niemeijer and Spiers, 2007; den Hartog and Spiers, 2013; Verberne et al., 2020), (4) transient increases in pore fluid pressure due to increased compaction rates at higher velocities (e.g., Faulkner et al., 2018), and (5) shear-induced dehydration of phyllosilicate minerals in the gouge layer (e.g., Takahashi et al., 2011; Okazaki and Katayama, 2015; Leclère et al., 2016). We conclude that velocity dependent water film thickness is most consistent with our data. Specifically, growth in the real area of asperity contacts due to plastic deformation should result in temperature-dependent values of b (e.g., Lu and He, 2014). However, this is not shown in our data, though we acknowledge that small temperature effects on b may be masked by the influence of strain-hardening. Furthermore, our sample contains >97% chlorite and we observe no microstructural evidence of pressure solution (Fig. 7). Transient increases in pore fluid pressure are also unlikely to influence the frictional behavior of our sample at low slip rates (<1 μm/s) where the highest values of b are measured. Finally, our experiments were conducted well below the thermal stability limit of chlorite (~650 °C), and we observe no evidence for the formation of dehydration products in our deformed samples.

We propose that the magnitude of b and its velocity dependence are controlled by the time-dependent removal of adsorbed water films from mineral surfaces (e.g., Scruggs, 1997). Likewise, Okamoto et al. (2019) suggested that the increase in steady state frictional strength of chlorite with temperature may result from the effect of adsorbed water films, which is also consistent with our observations. Adsorbed water coats grain surfaces and decreases the strength and/or real area of their contacts. We propose that at lower sliding velocities, the average grain contact lifetime is longer, allowing for more time for water layers to squeeze out and cause strengthening. Thinner water layers at grain contacts may lead to higher strength for two reasons. First, the shear strength of structured water layers between grains increases with decreasing layer thickness (Israelachvili et al., 1988). In addition, thinner water layers may also result in a larger real area of contact between rough grain surfaces, thereby increasing frictional resistance at low sliding rates. As such, we infer that either or both these processes may control the negative rate dependence of b (Fig. 5) and overall rate-weakening behavior of chlorite at 70 MPa and 120 MPa effective pressure. However, conditions of high pore fluid pressure or low effective pressure may allow adsorbed water films to maintain their thickness (e.g., Van Diggelen et al., 2010; Behnsen and Faulkner, 2012), which would decrease the evolution effect. Our observation that chlorite exhibits large rate-strengthening and state-insensitive frictional behavior during slower rate steps (0.001 to 1 μm/s) only at 120 MPa pore pressure ($\sigma_3' = 10$ MPa) (Fig. 2c) seems to support this interpretation. Additionally, recent experiments using faster velocity steps (>0.1 μm/s) also showed that increasing pore fluid pressure promotes greater rate-strengthening behavior and near-zero or negative b values in phyllosilicate-rich gouges, even at constant effective pressure (Xing et al., 2019; Bedford et al., 2021). However, we note from our high pore fluid pressure experiments (G0019 and G0202) that increasing shear strain and fabric development also influence the frictional behavior of chlorite. Therefore, further experimental studies are required to fully constrain the effects of fabric evolution and pore fluid pressure on the slip behavior of phyllosilicates at low velocities.

4.3. *Synthesis*

At relatively fast slip rates (>0.1 μm/s), our measurements of chlorite constitutive properties, including its temperature-strengthening and velocity-strengthening frictional behavior, are consistent with results from previous experimental studies (Okamoto et al., 2019; Fagereng and Ikari, 2020; Ikari et al., 2009). However, we also observe that chlorite transitions to rate-neutral or -weakening behavior at slip rates below 0.1 μm/s. Based on microstructural and micromechanical analyses, we interpret that this transition in rate dependence is controlled by a competition between mineral deformation mechanisms at grain contacts (subcritical fracture and delamination), which increase *a*, and the time-dependent properties of water films bonded to contacts, which increase *b*.

By comparing the frictional properties of chlorite with other phyllosilicates, we find that at low velocities, the rate dependence and temperature dependence of strength are often inversely correlated. For instance, illite, which strengthens with increasing temperature from room temperature to 200 °C (Kubo and Katayama, 2015), is predicted to velocity-weaken at slip rates slower than 0.1 μm/s (den Hartog et al., 2012) similar to our results for chlorite at 25 °C. Conversely, water-saturated phyllosilicates that show temperature-weakening or -neutral friction (e.g., antigorite, talc, smectite, muscovite, and biotite) all rate-strengthen at low velocities (~0.001 to 0.01 μm/s) (Reinen et al., 1992; Moore and Lockner, 2008; Coble et al., 2014; Scruggs and Tullis, 1998). We hypothesize that phyllosilicates rate-weaken at low deformation rates when they are temperature-strengthening because both responses are controlled by physical changes of water films bonded to mineral surfaces. Although chlorite and possibly illite seem to be unique in promoting velocity-neutral or -weakening behavior of faults at shallow crustal levels corresponding to <200 °C, other phyllosilicates may transition to similar behavior at higher temperatures. For example, water-saturated biotite and muscovite transition to temperature-strengthening behavior above 100 to 200 °C, which may promote rate-weakening friction at low deformation rates, as has been documented at even higher velocities and temperatures (Lu and He, 2014; Van Diggelen et al., 2010). In contrast, both oven-dried and water-saturated talc continue to temperature-weaken and exhibit large rate-strengthening behavior at low deformation rates (0.01 μm/s) from 100 to 300 °C, which likely reflects its hydrophobic nature (Moore and Lockner, 2008). Lastly, chlorites tested by Moore and Lockner (2015) were reported to rate-strengthen at similar shearing rates (0.00115 to 1 μm/s) as our experiments and exhibit no clear temperature dependence of strength from 25 to 300 °C, which also supports the hypothesis that phyllosilicates rate-weaken at low velocities when they are temperature-strengthening. However, the discrepancy between chlorite constitutive behavior in our study and that reported by Moore and Lockner (2015) may imply that other factors besides temperature and shearing rate determine whether adsorbed water films affect the slip behavior of chlorite, such as pore fluid pressure or Fe content.

4.4. *Implications for natural fault zones*

Chlorite is frictionally weak (μ ~ 0.4) under shallow hydrothermal conditions (Fig. 2), and faults containing chlorite may therefore accommodate slip under low shear stresses. This finding is consistent with field observations of chlorite-bearing fault zones in which deformation is localized into contiguous layers of chlorite-rich fault rock (e.g., Lacroix et al., 2012; Phillips et al., 2020; Fagereng and Ikari, 2020). However, the increase in frictional strength of chlorite with increasing temperature indicates that fault zones enriched in chlorite may become stronger with increasing depth. This relationship may extend to depths corresponding to the thermal stability limit of chlorite, as the frictional strength of chlorite is shown to increase with temperature up to 600 °C (Okamoto et al., 2019). In addition, we observe that chamosite which is the Fe^{2+} endmember of chlorite displays higher values of friction than what has been reported for clinochlore, its Mg-rich counterpart (Okamoto et al., 2019). This comparison between the strengths of Fe- and Mg-rich chlorites is consistent with previous trends observed by Moore and Lockner (2015), indicating that faults enriched in Fe-rich chlorite may be stronger than faults filled with Mg-rich chlorite.

The constitutive behavior of chlorite has important implications for the stability of chlorite-rich fault zones. Based on previous laboratory measurements, chlorite has been interpreted to exhibit predominantly stable, rate-strengthening behavior across a wide range of pressure and temperature conditions, indicating that it will promote aseismic creep from shallow to deep segments of faults (Ikari et al., 2009; Okamoto et al., 2019; Fagereng and Ikari, 2020). However, while we observe rate-strengthening behavior of chlorite at typical shearing velocities used in friction experiments (>10^{-6} m/s), we observe that chlorite exhibits rate-neutral to rate-weakening behavior when sheared at slower natural rates of fault slip (10^{-9} to 10^{-7} m/s) (Fig. 4a). This suggests that faults enriched in chlorite may be more easily destabilized than previously thought. Furthermore, this rate-weakening behavior of chlorite occurs within the characteristic slip rates of slow slip events (~10^{-8} to 10^{-7} m/s). One of the proposed causes of slow slip is a transition between rate-strengthening and slightly rate-weakening behavior during frictional sliding (Rubin, 2008; Liu and Rice, 2009; Segall et al., 2010), and chlorite is a product of metasomatism at shallow and deep slow slip conditions (Phillips et al., 2020; Braden and Behr, 2021). Thus, faults enriched in chlorite may become marginally unstable at slow slip rates but stabilize at a cutoff velocity around 1 μm/s (as modelled by Kato (2003), Shibazaki and Iio (2003), and Liu and Rice (2009)). Although our study focuses on chlorite deformation at shallow depths within fault zones, chlorite may also play a significant role on slow slip within the deep tremor source of subduction zones, wherein chlorite is present and chlorite and lawsonite are predicted to dehydrate and generate high pore fluid pressures (French and Condit, 2019; Condit et al., 2020).

5. Conclusions

Chlorite is an important product of hydrothermal alteration within fault zones, including transform and subduction plate boundaries. However, it is poorly studied compared to other phyllosilicate minerals, particularly under elevated temperatures and at low sliding velocities. We present the results of triaxial shear experiments conducted at constant confining pressure of 130 MPa, pore fluid pressures from 10 to 120 MPa, and temperatures from 25 to 130 °C. We show that chlorite has a frictional strength that increases by Δμ ~ 0.06 as temperature increases from 25 to 130 °C. At velocities less than 1 μm/s the chlorite is rate-weakening and it transitions to rate-strengthening at higher velocities. Overall, the magnitude of the rate-dependence is greatest at 25 °C. These results indicate that seismic and slow slip may nucleate in chlorite-rich fault zones. We attribute the magnitude of the instantaneous rate dependence (*a*) to rate-strengthening mineral deformation and the magnitudes of the evolution effect (*b*) and the overall rate-dependence of the frictional strength (*a*-*b*) to the strength of water films between grains.

Supplementary data to this article can be found online at https://doi.org/10.1016/j.tecto.2022.229435.

CRediT authorship contribution statement

Benjamin D. Belzer: Conceptualization, Methodology, Formal analysis, Investigation, Writing – original draft, Visualization. **Melodie E. French:** Conceptualization, Writing – review & editing, Supervision, Funding acquisition.

Declaration of Competing Interest

The authors declare that they have no known competing financial interests or personal relationships that could have appeared to influence the work reported in this paper.

Acknowledgements

This work was funded by NSF EAR-1759127 to MF. The use of the EPMA facility at the Department of Earth Science, Rice University, Houston, TX is kindly acknowledged, and we thank Gabi Costin for his assistance. We thank Diane Moore and an anonymous reviewer for the constructive comments that helped to improve the manuscript.

Appendix A. Jacket strength

The three polyolefin jackets we used for our experiments impart additional shear resistance during slip. To calibrate the strength of the jackets as a function of displacement and temperature, we deformed stacks of two ungreased lead shims at 25 °C and 130 °C using the same saw-cut configuration, jacketing assembly, and confining pressure as our gouge experiments. Jacket strength was measured at a shear velocity of 1 μm/s, following other friction studies that have calibrated the strength of jacketing materials using a single displacement rate (e.g., Tembe et al., 2010; Coble et al., 2014). We also imposed velocity steps between 1 and 10 μm/s during the room temperature test. However, we were unable to measure the effect of slip rate on jacket strength due to the highly rate-sensitive behavior of the lead shims.

During jacket tests at room temperature and 130 °C, the samples yielded under differential stresses of 10 MPa and 5 MPa, respectively, and then hardened steadily with slip (Fig. A.1). These yield strengths are consistent with reported flow stresses of lead cores at equivalent temperatures and strain rates when corrected for sample geometry (Hotta et al., 2007; Paterson and Olgaard, 2000). Thus, we attributed the yield point to plastic deformation of the lead shims and the subsequent strain hardening behavior to the displacement-dependent strength of the jackets. We calibrated jacket strength by taking a least squares fit of the change in differential stress with displacement, omitting the fast velocity steps during the room temperature experiment. We obtained slopes of 1.55 MPa/mm at room temperature and 0.58 MPa/mm at 130 °C.

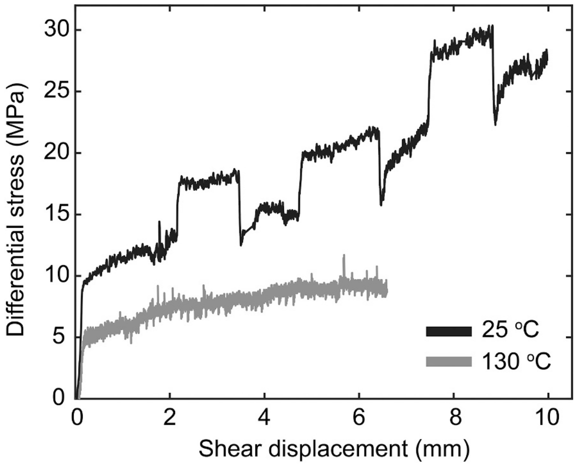

Fig. A.1. Results of jacket strength calibration tests using lead shims deformed at room temperature and 130 °C.

Appendix B. Pore volume changes

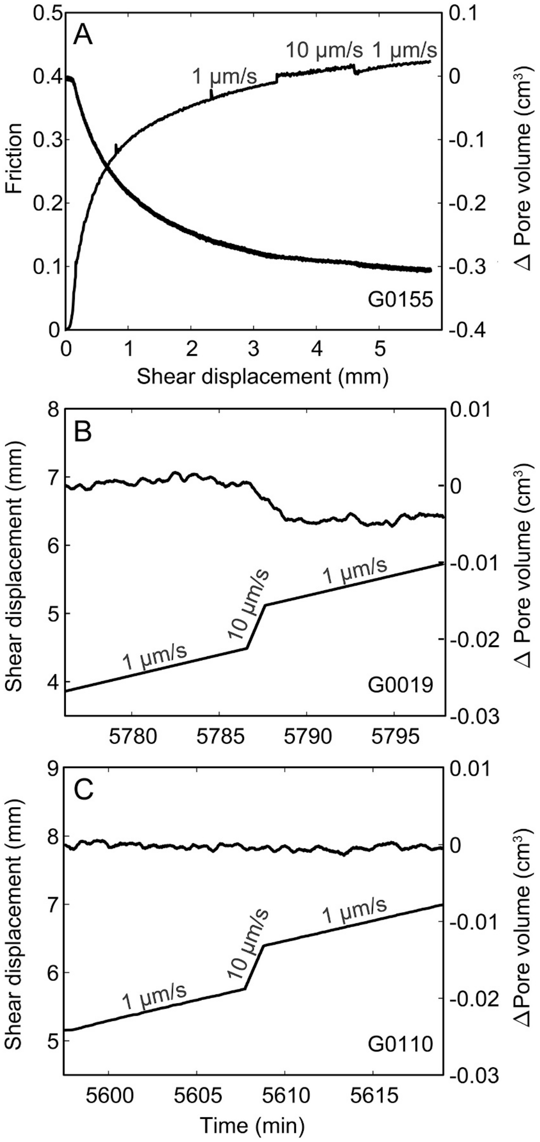

Fig. B.1. Measurements of pore volume change during three experiments: (a) compaction during the fast rate-stepping friction test (G0155), (b) normalized pore volume changes showing greater compaction at the 10 μm/s rate step in sample G0019 (10 MPa effective pressure) and a 64 s lag time in pore volume response after velocity is stepped down again to 1 μm/s; (c) sample G0110 showing no evidence of pore volume change at the 10 μm/s rate step.

References

Bedford, J.D., Faulkner, D.R., Allen, M.J., Hirose, T., 2021. The stabilizing effect of high pore-fluid pressure along subduction megathrust faults: evidence from friction experiments on accretionary sediments from the Nankai Trough. Earth Planet. Sci. Lett. 574, 117161 https://doi.org/10.1016/j.epsl.2021.117161.

Beeler, N.M., Tullis, T.E., Kronenberg, A.K., Reinen, L.A., 2007. The instantaneous rate dependence in low temperature laboratory rock friction and rock deformation experiments. J. Geophys. Res. Solid Earth 112 (B7). https://doi.org/10.1029/2005JB003772.

Behnsen, J., Faulkner, D.R., 2012. The effect of mineralogy and effective normal stress on frictional strength of sheet silicates. J. Struct. Geol. 42, 49–61. https://doi.org/10.1016/j.jsg.2012.06.015.

Beynon, S.J., Faulkner, D.R., 2020. Dry, damp, or drenched? The effect of water saturation on the frictional properties of clay fault gouges. J. Struct. Geol. 140, 104094 https://doi.org/10.1016/j.jsg.2020.104094.

Blanpied, M.L., Tullis, T.E., Weeks, J.D., 1998. Effects of slip, slip rate, and shear heating on the friction of granite. J. Geophys. Res. Solid Earth 103 (B1), 489–511. https://doi.org/10.1029/97JB02480.

Braden, Z., Behr, W.M., 2021. Weakening mechanisms in a basalt-hosted subduction megathrust fault segment, southern Alaska. J. Geophys. Res. Solid Earth 126 (9). https://doi.org/10.1029/2021JB022039.

Byerlee, J., 1978. Friction of rocks. In: Rock Friction and Earthquake Prediction. Birkhäuser, Basel, pp. 615–626.

Carpenter, B.M., Saffer, D.M., Marone, C., 2012. Frictional properties and sliding stability of the San Andreas fault from deep drill core. Geology 40 (8), 759–762. https://doi.org/10.1130/G33007.1.

Chester, F.M., 1994. Effects of temperature on friction: constitutive equations and experiments with quartz gouge. J. Geophys. Res. Solid Earth 99 (B4), 7247–7261. https://doi.org/10.1029/93JB03110.

Chester, F.M., 1995. A rheologic model for wet crust applied to strike-slip faults. J. Geophys. Res. Solid Earth 100 (B7), 13033–13044. https://doi.org/10.1029/95JB00313.

Chester, F.M., Higgs, N.G., 1992. Multimechanism friction constitutive model for ultrafine quartz gouge at hypocentral conditions. J. Geophys. Res. Solid Earth 97 (B2), 1859–1870 of Geophysical Research: Solid Earth, 115(B3). https://doi.org/10.1029/91JB02349.

Coble, C.G., French, M.E., Chester, F.M., Chester, J.S., Kitajima, H., 2014. In situ frictional properties of San Andreas Fault gouge at SAFOD. Geophys. J. Int. 199 (2), 956–967. https://doi.org/10.1093/gji/ggu306.

Collettini, C., Niemeijer, A., Viti, C., Marone, C., 2009. Fault zone fabric and fault weakness. Nature 462 (7275). https://doi.org/10.1038/nature08585.

Condit, C.B., Guevara, V.E., Delph, J.R., French, M.E., 2020. Slab dehydration in warm subduction zones at depths of episodic slip and tremor. Earth Planet. Sci. Lett. 552 https://doi.org/10.1016/j.epsl.2020.116601.

den Hartog, S.A., Spiers, C.J., 2013. Influence of subduction zone conditions and gouge composition on frictional slip stability of megathrust faults. Tectonophysics 600, 75–90. https://doi.org/10.1016/j.tecto.2012.11.006.

den Hartog, S.A.M., Niemeijer, A.R., Spiers, C.J., 2012. New constraints on megathrust slip stability under subduction zone P–T conditions. Earth Planet. Sci. Lett. 353, 240–252. https://doi.org/10.1016/j.epsl.2012.08.022.

den Hartog, S.A.M., Niemeijer, A.R., Spiers, C.J., 2013. Friction on subduction megathrust faults: beyond the illite–muscovite transition. Earth Planet. Sci. Lett. 373, 8–19. https://doi.org/10.1016/j.epsl.2013.04.036.

Dieterich, J.H., 1979. Modeling of rock friction: 1. Experimental results and constitutive equations. J. Geophys. Res. Solid Earth 84 (B5), 2161–2168. https://doi.org/10.1029/JB084iB05p02161.

Dieterich, J.H., 1981. Constitutive properties of faults with simulated gouge. In: Mechanical Behavior of Crustal Rocks, 24, pp. 103–120.

Dieterich, J.H., Conrad, G., 1984. Effect of humidity on time-and velocity-dependent friction in rocks. J. Geophys. Res. Solid Earth 89 (B6), 4196–4202. https://doi.org/10.1029/JB089iB06p04196.

Fagereng, Å., Ikari, M.J., 2020. Low-temperature frictional characteristics of chlorite-epidote-amphibole assemblages: implications for strength and seismic style of retrograde fault zones. J. Geophys. Res. Solid Earth 125 (4). https://doi.org/10.1029/2020JB019487.

Faulkner, D.R., Rutter, E.H., 2003. The effect of temperature, the nature of the pore fluid, and subyield differential stress on the permeability of phyllosilicate-rich fault gouge. J. Geophys. Res. Solid Earth 108 (B5). https://doi.org/10.1029/2001JB001581.

Faulkner, D.R., Lewis, A.C., Rutter, E.H., 2003. On the internal structure and mechanics of large strike-slip fault zones: field observations of the Carboneras fault in southeastern Spain. Tectonophysics 367 (3–4), 235–251. https://doi.org/10.1016/S0040-1951(03)00134-3.

Faulkner, D.R., Sanchez-Roa, C., Boulton, C., Den Hartog, S.A.M., 2018. Pore fluid pressure development in compacting fault gouge in theory, experiments, and nature. J. Geophys. Res. Solid Earth 123 (1), 226–241. https://doi.org/10.1002/2017JB015130.

French, M.E., Condit, C.B., 2019. Slip partitioning along an idealized subduction plate boundary at deep slow slip conditions. Earth Planet. Sci. Lett. 528 https://doi.org/10.1016/j.epsl.2019.115828.

French, M.E., Chester, F.M., Chester, J.S., 2015. Micromechanisms of creep in clay-rich gouge from the Central Deforming Zone of the San Andreas Fault. J. Geophys. Res. Solid Earth 120 (2), 827–849. https://doi.org/10.1002/2014JB011496.

Haines, S.H., Kaproth, B., Marone, C., Saffer, D., Van der Pluijm, B., 2013. Shear zones in clay-rich fault gouge: a laboratory study of fabric development and evolution. J. Struct. Geol. 51, 206–225. https://doi.org/10.1016/j.jsg.2013.01.002.

He, C., Luo, L., Hao, Q.M., Zhou, Y., 2013. Velocity-weakening behavior of plagioclase and pyroxene gouges and stabilizing effect of small amounts of quartz under hydrothermal conditions. J. Geophys. Res. Solid Earth 118 (7), 3408–3430. https://doi.org/10.1002/jgrb.50280.

Hotta, S., Matsumoto, K., Murakami, T., Narushima, T., Ouchi, C., 2007. Dynamic and static restoration behaviors of pure lead and tin in the ambient temperature range. Mater. Trans. 0709030188 https://doi.org/10.2320/matertrans.MRA2007078.

Ikari, M.J., Kopf, A.J., 2017. Seismic potential of weak, near-surface faults revealed at plate tectonic slip rates. Sci. Adv. 3 (11) https://doi.org/10.1126/sciadv.1701269.

Ikari, M.J., Saffer, D.M., Marone, C., 2007. Effect of hydration state on the frictional properties of montmorillonite-based fault gouge. J. Geophys. Res. Solid Earth 112 (B6). https://doi.org/10.1029/2006JB004748.

Ikari, M.J., Saffer, D.M., Marone, C., 2009. Frictional and hydrologic properties of clay-rich fault gouge. J. Geophys. Res. Solid Earth 114 (B5). https://doi.org/10.1029/2008JB006089.

Israelachvili, J.N., McGuiggan, P.M., Homola, A.M., 1988. Dynamic properties of molecularly thin liquid films. Science 240 (4849), 189–191. https://doi.org/10.1126/science.240.4849.189.

Jefferies, S.P., Holdsworth, R.E., Wibberley, C.A.J., Shimamoto, T., Spiers, C.J., Niemeijer, A.R., Lloyd, G.E., 2006. The nature and importance of phyllonite development in crustal-scale fault cores: an example from the Median Tectonic Line, Japan. J. Struct. Geol. 28 (2), 220–235. https://doi.org/10.1016/j.jsg.2005.10.008.

Kato, N., 2003. A possible model for large preseismic slip on a deeper extension of a seismic rupture plane. Earth Planet. Sci. Lett. 216, 17–25. https://doi.org/10.1016/S0012-821X(03)00483-7.

Kawai, K., Sakuma, H., Katayama, I., Tamura, K., 2015. Frictional characteristics of single and polycrystalline muscovite and influence of fluid chemistry. J. Geophys. Res. Solid Earth 120 (9), 6209–6218. https://doi.org/10.1002/2015JB012286.

King, D.S.H., Marone, C., 2012. Frictional properties of olivine at high temperature with applications to the strength and dynamics of the oceanic lithosphere. J. Geophys. Res. Solid Earth 117 (B12). https://doi.org/10.1029/2012JB009511.

Kronenberg, A.K., Kirby, S.H., Pinkston, J., 1990. Basal slip and mechanical anisotropy of biotite. J. Geophys. Res. Solid Earth 95 (B12), 19257–19278. https://doi.org/10.1029/JB095iB12p19257.

Kubo, T., Katayama, I., 2015. Effect of temperature on the frictional behavior of smectite and illite. J. Mineral. Petrol. Sci. 110 (6), 293–299. https://doi.org/10.2465/jmps.150421.

Lacroix, B., Charpentier, D., Buatier, M., Vennemann, T., Labaume, P., Adatte, T., Dubois, M., 2012. Formation of chlorite during thrust fault reactivation. Record of fluid origin and P–T conditions in the Monte Perdido thrust fault (southern Pyrenees). Contrib. Mineral. Petrol. 163 (6), 1083–1102. https://doi.org/10.1007/s00410-011-0718-0.

Leclère, H., Faulkner, D., Wheeler, J., Mariani, E., 2016. Permeability control on transient slip weakening during gypsum dehydration: Implications for earthquakes in subduction zones. Earth Planet. Sci. Lett. 442, 1–12. https://doi.org/10.1016/j.epsl.2016.02.015.

Liu, Y., Rice, J.R., 2009. Slow slip predictions based on granite and gabbro friction data compared to GPS measurements in northern Cascadia. J. Geophys. Res. Solid Earth 114 (B9). https://doi.org/10.1029/2008JB006142.

Logan, J.M., Friedman, M., Higgs, N., Dengo, C., Shimamoto, T., 1979. Experimental studies of simulated gouge and their application to studies of natural fault zones. In: Proc. Conf. VIII. Analysis of Actual Fault Zones in Bedrock, U.S. Geol. Surv. Open File Rep., 79-1239, pp. 305–343. Washington, D. C.

Lu, Z., He, C., 2014. Frictional behavior of simulated biotite fault gouge under hydrothermal conditions. Tectonophysics 622, 62–80. https://doi.org/10.1016/j.tecto.2014.03.002.

MacLeod, C.J., Escartin, J., Banerji, D., Banks, G.J., Gleeson, M., Irving, D.H.B., Smith, D. K., 2002. Direct geological evidence for oceanic detachment faulting: the Mid-Atlantic Ridge, 15 45′ N. Geology 30 (10), 879–882. https://doi.org/10.1130/0091-7613(2002)030<0879:DGEFOD>2.0.CO;2.

Mares, V.M., Kronenberg, A.K., 1993. Experimental deformation of muscovite. J. Struct. Geol. 15 (9–10), 1061–1075. https://doi.org/10.1016/0191-8141(93)90156-5.

Marone, C., 1998. Laboratory-derived friction laws and their application to seismic faulting. Annu. Rev. Earth Planet. Sci. 26 (1), 643–696. https://doi.org/10.1146/annurev.earth.26.1.643.

Masel, R.I., 1996. Principles of Adsorption and Reaction on Solid Surfaces, vol. 3. John Wiley & Sons.

Moore, D.E., Lockner, D.A., 2004. Crystallographic controls on the frictional behavior of dry and water-saturated sheet structure minerals. J. Geophys. Res. Solid Earth 109 (B3) https://doi.org/10.1029/2003JB002582.

Moore, D.E., Lockner, D.A., 2007. Friction of the smectite clay montmorillonite: A review and interpretation of data. In: Dixon, T.H., Moore, C. (Eds.), The Seismogenic Zone of Subduction Thrust Faults, Margins Theoretical and Experimental Earth Science Series, vol. 2. Columbia Univ. Press, New York, pp. 317–345. https://doi.org/10.7312/dixo13866-011.

Moore, D.E., Lockner, D.A., 2008. Talc friction in the temperature range 25–400 C: Relevance for fault-zone weakening. Tectonophysics 449 (1–4), 120–132. https://doi.org/10.1016/j.tecto.2007.11.039.

Moore, D.E., Lockner, D.A., 2011. Frictional strengths of talc-serpentine and talc-quartz mixtures. J. Geophys. Res. Solid Earth 116 (B1). https://doi.org/10.1029/2010JB007881.

Moore, D.E., Lockner, D.A., 2015, December. Correlation of chlorite frictional strength with composition. In: AGU Fall Meeting Abstracts, Vol. 2015. MR21C-2628.

Moore, D.E., Rymer, M.J., 2007. Talc-bearing serpentinite and the creeping section of the San Andreas fault. Nature 448 (7155), 795–797. https://doi.org/10.1038/nature06064.

Moore, D.E., Summers, R., Byerlee, J.D., 1989. Sliding behavior and deformation textures of heated illite gouge. J. Struct. Geol. 11 (3), 329–342. https://doi.org/10.1016/0191-8141(89)90072-2.

Moore, D.E., Lockner, D.A., Ma, S., Summers, R., Byerlee, J.D., 1997. Strengths of serpentinite gouges at elevated temperatures. J. Geophys. Res. Solid Earth 102 (B7), 14787–14801. https://doi.org/10.1029/97JB00995.

Morrow, C.A., Shi, L.Q., Byerlee, J.D., 1984. Permeability of fault gouge under confining pressure and shear stress. J. Geophys. Res. Solid Earth 89 (B5), 3193–3200. https://doi.org/10.1029/JB089iB05p03193.

Morrow, C.A., Moore, D.E., Lockner, D.A., 2000. The effect of mineral bond strength and adsorbed water on fault gouge frictional strength. Geophys. Res. Lett. 27 (6), 815–818. https://doi.org/10.1029/1999GL008401.

Nakatani, M., 2001. Conceptual and physical clarification of rate and state friction: Frictional sliding as a thermally activated rheology. J. Geophys. Res. Solid Earth 106 (B7), 13347–13380. https://doi.org/10.1029/2000JB900453.

Newman, A.C.D., 1987. The interaction of water with clay mineral surfaces. In: Newman, A.C.D. (Ed.), Chemistry of Clays and Clay Minerals, Mineral. Soc. Monogr., Vol. 6. John Wiley, Hoboken, N. J, pp. 237–274.

Niemeijer, A.R., Spiers, C.J., 2007. A microphysical model for strong velocity weakening in phyllosilicate-bearing fault gouges. J. Geophys. Res. Solid Earth 112 (B10). https://doi.org/10.1029/2007JB005008.

Okamoto, A.S., Verberne, B.A., Niemeijer, A.R., Takahashi, M., Shimizu, I., Ueda, T., Spiers, C.J., 2019. Frictional properties of simulated chlorite gouge at hydrothermal conditions: implications for subduction megathrusts. J. Geophys. Res. Solid Earth 124 (5), 4545–4565. https://doi.org/10.1029/2018JB017205.

Okazaki, K., Katayama, I., 2015. Slow stick slip of antigorite serpentinite under hydrothermal conditions as a possible mechanism for slow earthquakes. Geophys. Res. Lett. 42 (4), 1099–1104. https://doi.org/10.1002/2014GL062735.

Paterson, M.S., Olgaard, D.L., 2000. Rock deformation tests to large shear strains in torsion. J. Struct. Geol. 22 (9), 1341–1358. https://doi.org/10.1016/S0191-8141(00)00042-0.

Phillips, N.J., Motohashi, G., Ujiie, K., Rowe, C.D., 2020. Evidence of localized failure along altered basaltic blocks in tectonic mélange at the updip limit of the seismogenic zone: implications for the shallow slow earthquake source. Geochem. Geophys. Geosyst. 21 (7) https://doi.org/10.1029/2019GC008839.

Rabinowitz, H.S., Savage, H.M., Skarbek, R.M., Ikari, M.J., Carpenter, B.M., Collettini, C., 2018. Frictional behavior of input sediments to the Hikurangi Trench, New Zealand. Geochem. Geophys. Geosyst. 19 (9), 2973–2990. https://doi.org/10.1029/2018GC007633.

Reinen, L.A., Weeks, J.D., 1993. Determination of rock friction constitutive parameters using an iterative least squares inversion method. J. Geophys. Res. Solid Earth 98 (B9), 15937–15950. https://doi.org/10.1029/93JB00780.

Reinen, L.A., Tullis, T.E., Weeks, J.D., 1992. Two-mechanism model for frictional sliding of serpentinite. Geophys. Res. Lett. 19 (15), 1535–1538. https://doi.org/10.1029/92GL01388.

Rice, J.R., Lapusta, N., Ranjith, K., 2001. Rate and state dependent friction and the stability of sliding between elastically deformable solids. J. Mech. Phys. Solids 49 (9), 1865–1898. https://doi.org/10.1016/S0022-5096(01)00042-4.

Rubin, A.M., 2008. Episodic slow slip events and rate-and-state friction. J. Geophys. Res. Solid Earth 113 (B11). https://doi.org/10.1029/2008JB005642.

Ruina, A., 1983. Slip instability and state variable friction laws. J. Geophys. Res. Solid Earth 88 (B12), 10359–10370. https://doi.org/10.1029/JB088iB12p10359.

Saffer, D.M., Marone, C., 2003. Comparison of smectite-and illite-rich gouge frictional properties: application to the updip limit of the seismogenic zone along subduction megathrusts. Earth Planet. Sci. Lett. 215 (1–2), 219–235. https://doi.org/10.1016/S0012-821X(03)00424-2.

Sánchez-Roa, C., Faulkner, D.R., Boulton, C., Jimenez-Millan, J., Nieto, F., 2017. How phyllosilicate mineral structure affects fault strength in Mg-rich fault systems. Geophys. Res. Lett. 44 (11), 5457–5467. https://doi.org/10.1002/2017GL073055.

Schleicher, A.M., Van Der Pluijm, B.A., Warr, L.N., 2012. Chlorite-smectite clay minerals and fault behavior: new evidence from the San Andreas Fault Observatory at Depth (SAFOD) core. Lithosphere 4 (3), 209–220. https://doi.org/10.1130/L158.1.

Scholz, C.H., 2019. The Mechanics of Earthquakes and Faulting, 3rd ed. Cambridge University Press, Cambridge, UK. https://doi.org/10.1017/9781316681473.

Scruggs, V.J., 1997. Frictional Constitutive Properties and Related Microstructures of Albite, Muscovite, Biotite and Talc. Brown University.

Scruggs, V.J., Tullis, T.E., 1998. Correlation between velocity dependence of friction and strain localization in large displacement experiments on feldspar, muscovite and biotite gouge. Tectonophysics 295 (1–2), 15–40. https://doi.org/10.1016/S0040-1951(98)00113-9.

Segall, P., Rubin, A.M., Bradley, A.M., Rice, J.R., 2010. Dilatant strengthening as a mechanism for slow slip events. J. Geophys. Res. Solid Earth 115 (B12). https://doi.org/10.1029/2010JB007449.

Shibazaki, B., Iio, Y., 2003. On the physical mechanism of silent slip events along the deeper part of the seismogenic zone. Geophys. Res. Lett. 30 (9) https://doi.org/10.1029/2003GL017047.

Skarbek, R.M., Savage, H.M., 2019. RSFit3000: a MATLAB GUI-based program for determining rate and state frictional parameters from experimental data. Geosphere 15 (5), 1665–1676. https://doi.org/10.1130/GES02122.1.

Smith, S.A.F., Tesei, T., Scott, J.M., Collettini, C., 2017. Reactivation of normal faults as high-angle reverse faults due to low frictional strength: Experimental data from the Moonlight Fault Zone, New Zealand. J. Struct. Geol. 105, 34–43. https://doi.org/10.1016/j.jsg.2017.10.009.

Takahashi, M., Uehara, S.I., Mizoguchi, K., Shimizu, I., Okazaki, K., Masuda, K., 2011. On the transient response of serpentine (antigorite) gouge to stepwise changes in slip velocity under high-temperature conditions. J. Geophys. Res. Solid Earth 116 (B10). https://doi.org/10.1029/2010JB008062.

Tembe, S., Lockner, D.A., Wong, T.F., 2010. Effect of clay content and mineralogy on frictional sliding behavior of simulated gouges: binary and ternary mixtures of quartz, illite, and montmorillonite. J. Geophys. Res. Solid Earth 115 (B3). https://doi.org/10.1029/2009JB006383.

Tesei, T., Collettini, C., Carpenter, B.M., Viti, C., Marone, C., 2012. Frictional strength and healing behavior of phyllosilicate-rich faults. J. Geophys. Res. Solid Earth 117 (B9). https://doi.org/10.1029/2012JB009204.

Tesei, T., Harbord, C.W.A., De Paola, N., Collettini, C., Viti, C., 2018. Friction of mineralogically controlled serpentinites and implications for fault weakness. J. Geophys. Res. Solid Earth 123 (8), 6976–6991. https://doi.org/10.1029/2018JB016058.

Tullis, T.E., Weeks, J.D., 1987. Micromechanics of frictional resistance of calcite. Eos Trans. AGU 68, 405.

Van Diggelen, E.W., De Bresser, J.H., Peach, C.J., Spiers, C.J., 2010. High shear strain behaviour of synthetic muscovite fault gouges under hydrothermal conditions. J. Struct. Geol. 32 (11), 1685–1700. https://doi.org/10.1016/j.jsg.2009.08.020.

Verberne, B.A., Van Den Ende, M., Chen, J., Niemeijer, A.R., Spiers, C.J., 2020. The physics of fault friction: insights from experiments on simulated gouges at low shearing velocities. Solid Earth 11 (6). https://doi.org/10.5194/se-11-2075-2020.

Wintsch, R.P., Christoffersen, R., Kronenberg, A.K., 1995. Fluid-rock reaction weakening of fault zones. J. Geophys. Res. Solid Earth 100 (B7), 13021–13032. https://doi.org/10.1029/94JB02622.

Xing, T., Zhu, W., French, M., Belzer, B., 2019. Stabilizing effect of high pore fluid pressure on slip behaviors of gouge-bearing faults. J. Geophys. Res. Solid Earth 124 (9), 9526–9545. https://doi.org/10.1029/2019JB018002.